IGF26 - 26th International Conference on Fracture and Structural Integrity

Investigation of the biaxial flexural fracture of aluminosilicate glass by smeared fixed crack method

Zhen Wang[a,b]*, Andrea Manes[b]

[a]*Politecnico di Milano, Department of Mechanical Engineering, Milan 20156, Italy*
[b]*School of Aeronautics, Northwestern Polytechnical University, Xi'an 710072, Shaanxi, PR China*

Abstract

Ball-On-Ring (BOR) and Ring-On-Ring (ROR) tests are experimental methods used to characterize biaxial flexural strength of brittle materials. In this study, the quasi-static biaxial fracture behavior of aluminosilicate glass is investigated via BOR and ROR tests aided by a three-dimensional Digital Image Correlation (3D-DIC) technique. The in-plane strain field and out of plane deformation distribution during the loading process can be obtained by this special-designed test system. A finite element modeling approach incorporating smeared crack model is chosen to represent the discontinuous macrocrack brittle behavior of aluminosilicate glass. The simulations are conducted using the commercial software LS-DYNA with the implemented material model MAT280_GLASS. This numerical method is carefully assessed, and the capability of this model is evaluated by comparing the results of the numerical simulations with the corresponding experimental results.

Keywords: Aluminosilicate glass; Ball-On-Ring; Ring-On-Ring; Smeared crack method

1. Introduction

Silicate glass structures are widely used in buildings, vehicles, airplanes and electronic devices due to the unique transparency property. Biaxial flexural stress states are frequently encountered in these structures during service. (Deland et al., 2020) As silicate glass is a typical brittle material, the sudden failure of glass structures will cause

---

* Corresponding author. Tel.: ++39-02 2399 8630; fax: ++39-02 2399 8263.
E-mail address: zhen.wang@polimi.it

property damage and even human casualties. For the reliable operation and efficient design of these structures, it's essential to better understand their fracture and failure behavior under biaxial flexure.

Finite element method (FEM) is an efficient tool for deformation and stress analysis of engineering structures. As for brittle materials, crack initiation and propagation usually happen when the failure strength is reached. Several approaches have been developed to describe cracks in solids. Element deletion can be assigned to the elements reaching the failure criteria. (Pelfrene et al., 2016) This method is very simple and widely used to avoid element distortion problems. However, deleting elements directly from the numerical model is a non-physical process violating the conservation of mass and energy. A coupled finite element and smoothed particle hydrodynamics (SPH) method has been developed and is used in fracture problems of ceramics (Scazzosi et al., 2020), glass (Wang et al., 2021b) and rock (Mardalizad et al., 2020), in which eroded elements are replaced by SPH particles inheriting the mass and energy of solid elements. Cohesive zone method is also a very popular method for brittle materials simulations. (Vocialta et al., 2018; Wang et al., 2021a) Zero-thickness cohesive elements can be inserted into every two solid elements to represent the potential cracks. These cohesive elements obey the traction-separation law and will be deleted once the failure criteria are met. Recently, some meshless methods have also been developed for brittle fracture simulations, such as the discrete element method (DEM) (You et al., 2021) and the element-free Galerkin method (EFG) (Ma et al., 2020). However, when meshless methods or cohesive element method are used, the calculation efficiency is still much lower than FEM (Wang et al., 2021b). For large engineering structures, an extremely high number of cohesive elements or particles should be used, which will take up a lot of time and computing resources. Thus, FEM simulations are usually preferred for structure analysis.

In this study, the smeared fixed crack method is utilized to simulate the biaxial flexural behavior of aluminosilicate glass. In section 2, two experimental methods including BOR and ROR are introduced, together with a brief description of the experimental setups. The numerical method and parameters calibration process will be delivered in section 3, followed by the detailed discussion of the simulation results and the comparison with experiments. In the last section 5, some useful conclusions are drawn.

2. Experimental tests

The specimens produced from 6 mm thick aluminosilicate glass plates are disc samples with a diameter of 122 mm. The same specimens are used for both BOR and ROR tests, two common biaxial flexural methods. For BOR tests, the flexural strength σ_{BOR} can be calculated by (de With and Wagemans, 1989)

$$\sigma_{BOR} = \frac{3P(1+\mu)}{4\pi h^2}\left[1 + 2ln\left(\frac{R_s}{b}\right) + \frac{1-\mu}{1+\mu}\left(1 - \frac{b^2}{2R_s^2}\right)\frac{R_s^2}{R^2}\right] \tag{1}$$

where P is the peak load and μ is the Poisson's ratio. R, R_S and h represent the radius of specimen, radius of support ring, thickness of specimen respectively. The equivalent radius of the contact area between the ball and specimen b can be calculated by

$$b = \begin{cases} z, & for\ z > 1.724h \\ (1.6z^2 + h^2)^{1/2} - 0.675h, & for\ z < 1.724h \\ 0.325h, & for\ z \to 0 \end{cases} \tag{2}$$

where z is the actual contact radius of the contact area. According to the Hertz elastic contact stress equation

$$z = \left(3\,Pr/4\,E'\right)^{\frac{1}{3}} \tag{3}$$

where r is the radius of loading ball and E' is the equivalent Young's modulus expressed by

$$E'^{-1} = \frac{1-\mu_1^2}{E_1} + \frac{1-\mu_2^2}{E_2} \tag{4}$$

where the subscribes 1 and 2 represent the loading ball and plate respectively. In our case, μ_1=0.3, μ_2=0.22, E_1=200 GPa, E_2=75 GPa, r=8 mm. Thus, z can be calculated as 0.624 mm, which is smaller than 1.724h. In this way, the equivalent contact radius b can be defined by equation (2) as 2.002 mm.

The ROR biaxial flexural strength σ_{ROR} can be calculated by means of the plate bending theory (Standard, 2005)

$$\sigma_{ROR} = \frac{3P}{2\pi h^2}\left[(1-\mu)\frac{R_S^2 - R_L^2}{2R^2} + (1+\mu)ln\frac{R_S}{R_L}\right] \tag{5}$$

where R_L represent the radius of the loading ring.

A universal electronic testing machine was utilized to load the specimens at a constant loading speed of 0.2 mm/min, which can be regarded as a quasi-static loading condition. It should be noted that 3D-DIC technique was employed to monitor the in-time displacement and strain development on the bottom side of the specimen during tests. The detailed information of the experimental tests can be found in (Wang et al., 2021c).

## 3. Numerical method

3.1. Smeared fixed crack model

The smeared fixed crack model firstly introduced by (Hillerborg et al., 1976) was used for the simulation in this study and this material model was implemented in the commercial software LS-DYNA as MAT280_GLASS. Only shell elements (Elform=2, under-integrated) can be used for this model at present. There should be a sufficient number of integration points over thickness of the shell elements, as shown in Figure 1 (a). If a certain number of IP in one element fail, the whole element will fail. The default value of NIPF=1 (number of failed through thickness integration points needed to fail all through thickness integration points) resembles the fact, that a crack in a glass plate immediately runs through the thickness. The underlying material behavior before failure is isotropic and linear elastic. Asymmetric (tension-compression dependent) failure happens as soon as one of the following plane stress failure criteria is not satisfied

$$\begin{cases} max\left(\frac{\sigma_1}{FT},\frac{\sigma_2}{FT}\right) < 1 & if\ \sigma_1 > 0\ and\ \sigma_2 > 0 \\ max\left(-\frac{\sigma_1}{FC}, -\frac{\sigma_2}{FC}\right) < 1 & if\ \sigma_1 < 0\ and\ \sigma_2 < 0 \\ \frac{\sigma_1}{FT} - \frac{\sigma_2}{FC} < 1 & if\ \sigma_1 > 0\ and\ \sigma_2 < 0 \\ -\frac{\sigma_1}{FT} + \frac{\sigma_2}{FC} < 1 & if\ \sigma_1 < 0\ and\ \sigma_2 > 0 \end{cases} \tag{6}$$

where principal stresses σ_1 and σ_2 are bounded by the defined tensile strength FT and compression strength FC. As soon as failure happens in the tensile regime, a crack occurs perpendicular to the maximum principal stress direction, as shown in Figure 1 (b). The crack direction in the integration point which failed first sets the direction for the whole element and a local crack coordinate system will be built. At this stage, the element can no longer bear tensile loads perpendicular to the direction of the first crack. However, it can still bear loads at the orthogonal direction and a second crack can form in the orthogonal direction. Another feature of this numerical method is that the cracks can open and close independently, instead of simply deleting elements in order to represent cracks. In this study, the strength data obtained from BOR and ROR tests are set as FT in the numerical simulations, while the quasi-static compression strength 600 MPa of aluminosilicate glass is used for FC.
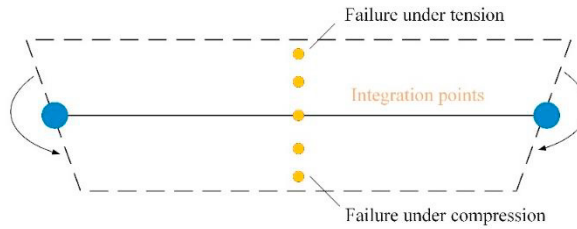
(a) Integration points along the thickness direction of the shell element
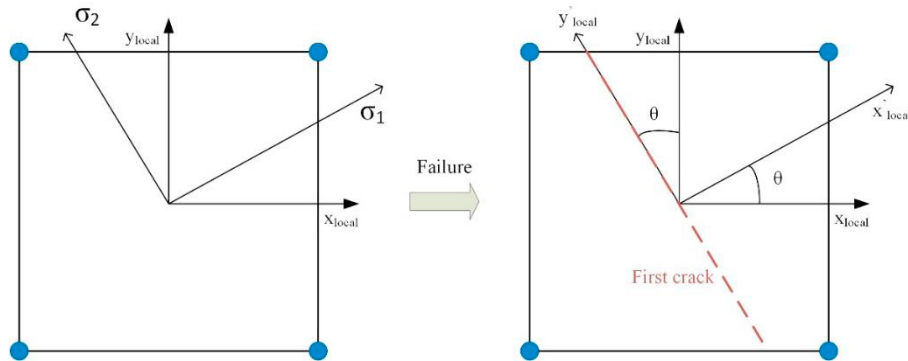
(b) Schematic of the failure process of one single element

Fig. 1. Smeared fixed crack numerical model.

The BOR and ROR numerical models are shown in Figure 2. Quarter models are provided here for convenience of showing the loading condition. However, full models were used in our numerical studies. Structured square meshes are used for the specimens and hexahedron solid meshes are used for the fixtures.
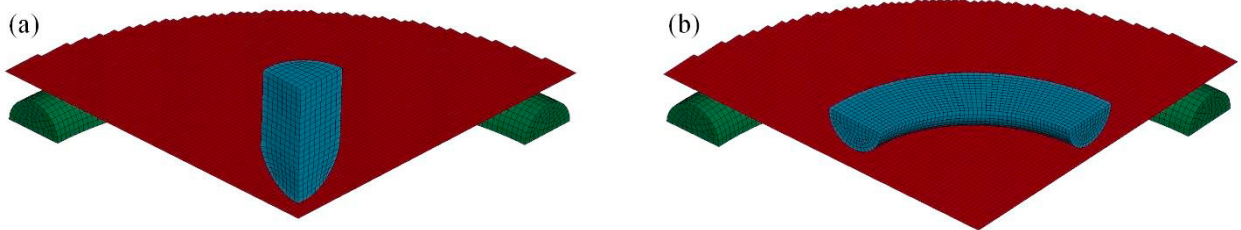

Fig. 2. (a) Ball-On-Ring model; (b) Ring-On-Ring model.

3.2. Effect of integration points

First of all, the effect of integration points on the simulated flexural strength of aluminosilicate glass plates were investigated, as shown in Figure 3. The dashed lines represent the experimental data. Numerical models with 3, 5, 7, 9 and 11 integration points were built and calculated respectively. With the increase of integration points along the thickness of the shell elements, the simulated flexural strength decreased and became stable. The stable values are comparable to experimental results for both BOR and ROR tests. The reason for this trend is that the integration points are far from the surface of the glass tile when less integration points are used, leading to the overestimation of strength data. It can also be seen from Figure 3 that with the increase of integration points, the calculation time increased. In order to balance the calculation efficiency and accuracy, nine integration points were used for BOR and ROR simulations in this work.
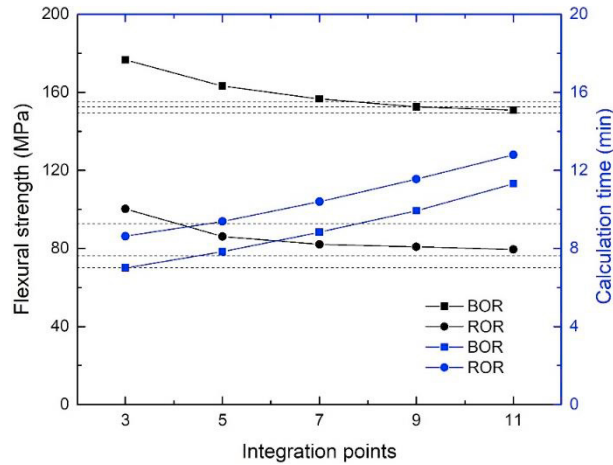
Fig. 3. Effect of integration points on the biaxial flexural strength and calculation time

3.3. Effect of mesh size

The mesh size sensitivity was also conducted, as shown in Figure 4. For the ROR loading condition, there is no apparent mesh size dependence at the mesh size range (0.4 mm – 1.2 mm) tested. For BOR models, the simulated flexural strength decreased slightly when the mesh size is smaller than 0.5mm due to the stress concentration induced by the point contact between indenter and specimen. It should be noted that with the decrease of mesh size, the calculation efficiency decreased remarkably. Finally, the mesh size 0.8 mm was chosen for the models in this study.
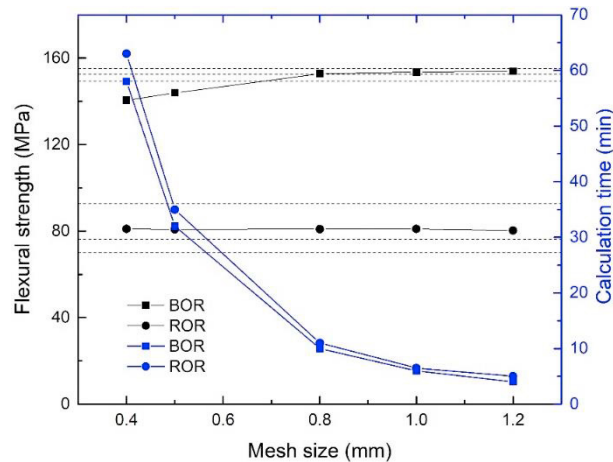

Fig. 4. Effect of mesh size on the biaxial flexural strength and calculation time

3.4. Effect of loading speed

As the smeared crack model (MAT280_GLASS) can only be used in explicit analysis in LS-DYNA, the numerical loading time must be sufficiently long to avoid dynamic effects for this quasi-static loading condition. (Wang et al., 2015) In real experimental tests, the loading speed is very low with a long loading time, which is actually unacceptable to be adopted for numerical simulations. In order to determine an appropriate numerical loading speed, different loading speeds from 0.025 m/s to 0.2 m/s were tried, as shown in Figure 5. With the decrease of loading speed, less fluctuations can be observed from the curves. In order to balance the calculation efficiency and accuracy, the loading speed 0.05 m/s was used for the simulations in this study.
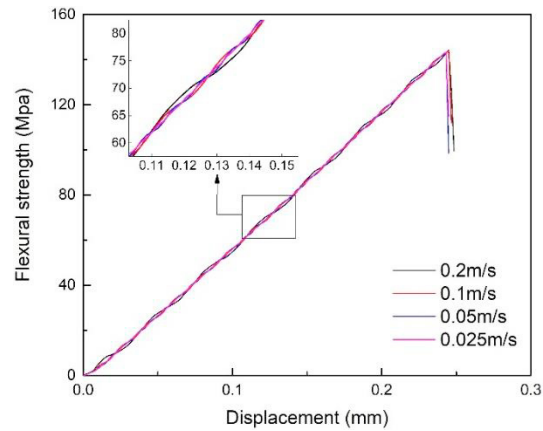
Fig. 5. Effect of loading speed on the biaxial flexural strength – displacement curve

4. Results and discussion
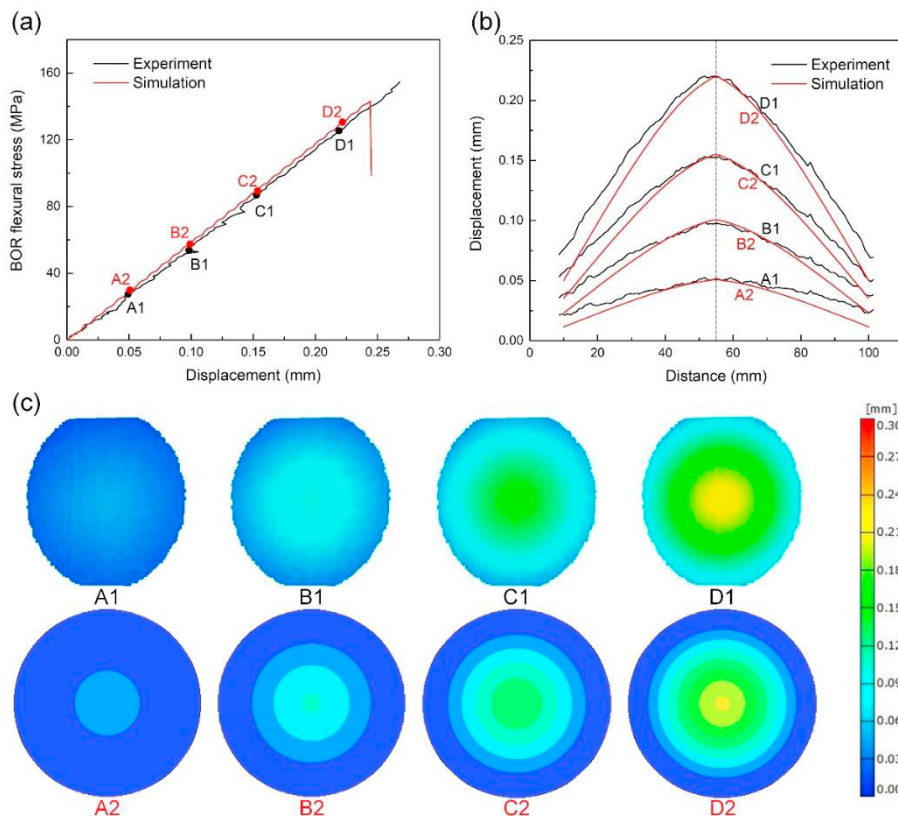
4.1. Deformation field

Fig. 6. Comparison between BOR test and simulation. (a) flexural stress-displacement curve; (b) out-of-plane displacement at different stages; (c) full-field out-of-plane displacement from DIC and simulation.

The comparison between typical BOR and ROR tests and numerical results are shown in Figures 6 and 7 respectively. For both loading conditions, the flexural stress - displacement relation is linear elastic. The

deformation field of specimens at different stages during loading process is also provided and fully comparable to numerical results. The comparison of force - displacement curves for BOR and ROR tests is provided in Figure 8. It can be seen from Figures 8 that both the peak fracture force, maximum displacement and stiffness of ROR specimen are higher than BOR specimen, meaning that much larger external work was applied to ROR specimen during the loading process. For BOR tests, there is only a small area under biaxial bending bellow the indenter. While there is a much bigger biaxial bending area for ROR tests. With the increase of the biaxial bending area, the stiffness and peak force will also increase as more strain energy is stored in the specimens. For both BOR and ROR tests, the center point bears the maximum displacement upon failure.
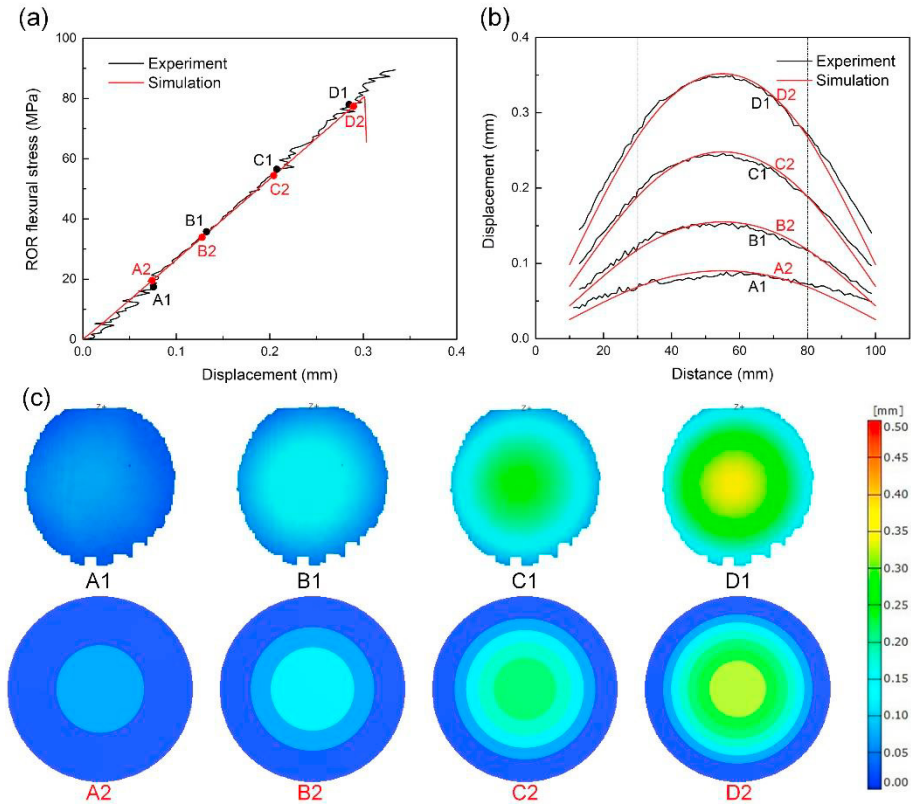

Fig. 7. Comparison between ROR test and simulation. (a) Flexural stress-displacement curve; (b) Out-of-plane displacement at different stages; (c) Full-field out-of-plane displacement from DIC and simulation.
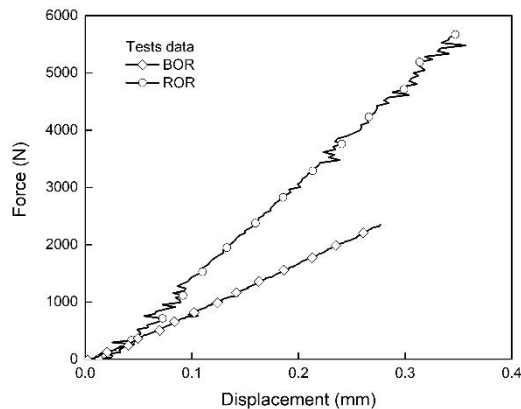

Fig. 8. Comparison of the force - displacement curves between BOR and ROR tests

4.2. Maximum principal stress and strain

The simulated maximum principal stress is provided in Figure 9. For BOR loading condition, there is a gradient distribution of maximum principal stress along the radius direction of the specimen. The peak value appears only at the very center of the plate, where biaxial flexural stress is applied. However, a uniform biaxial flexural stressed area can be observed below the loading ring during the ROR loading condition. It should be noted that both the principal stress distribution of BOR and ROR simulations are taken from the stage upon failure of the numerical models and the flexural strength of glass plates under BOR loading condition is higher than ROR.

In Figure 10 the major principal strain distribution along the specimen diameter between DIC measurement and simulations are compared. It can be seen that the curves from the tests are very fluctuated. On one hand, the measured strain is very small (<0.2%) and it is thus hard to measure small strains, while on the other hand, calculating strain is a differential process, which is more sensitive to the accumulative errors. Although there are fluctuations in the experimental curves, the major strain distribution and peak value are fully comparable between experiments and simulations. The BOR loading condition results in a gradient strain distribution on the glass surface, with the peak strain value in the center of the specimen. In contrast, a uniform strain distribution field is formed below the load ring for the ROR specimens. The maximum major strain for glass plates under BOR loading is higher than ROR. The possible reason for this difference during experiments are the randomly distributed surface flaws on glass plates. (Wereszczak et al., 2014) For ROR tests, many flaws are likely to be within the area of biaxial bending area as the area is quite big compared to the size of flaws. For BOR tests, the biaxial bending area is only a very small area below the indenter. Thus, the maximum major strain of specimens under BOR loading should be higher than ROR.
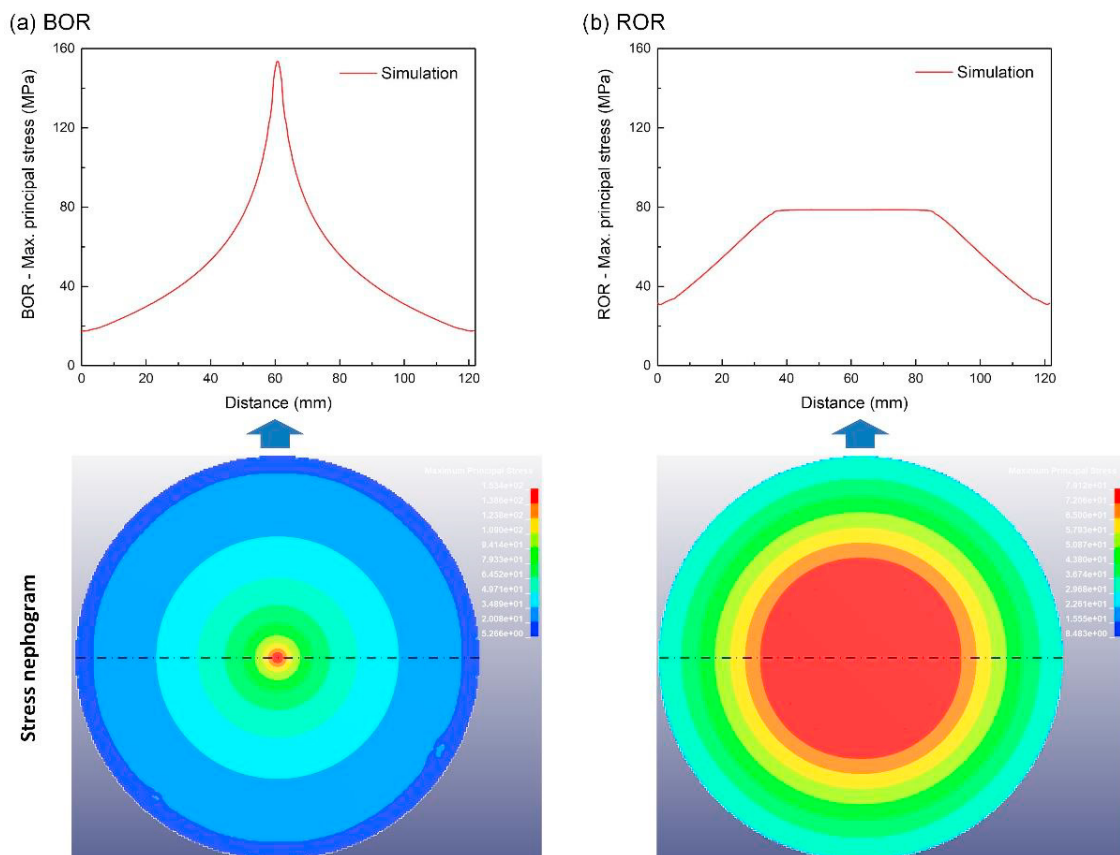

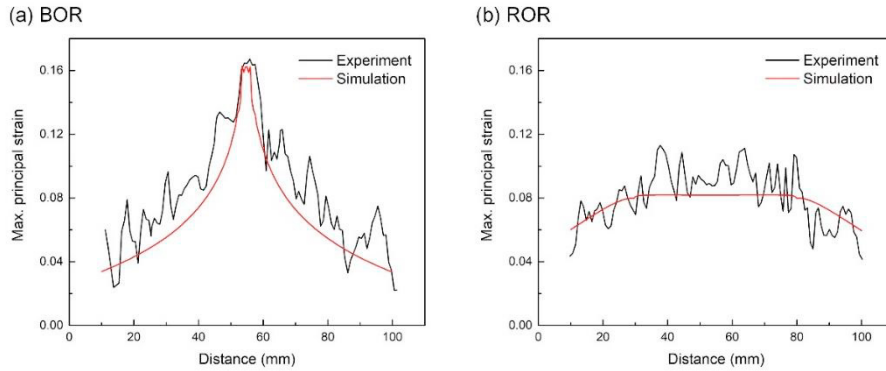Fig. 9. Maximum principal stress from (a) BOR and (b) ROR simulations

Fig. 10. Comparison of maximum principal strain for (a) BOR and (b) ROR tests

4.3. Fracture and failure modes

The fracture and failure modes of glass are important information for glass engineers to determine the fracture origin, loading conditions and evaluate the material strength. (Quinn, 2016) The typical fracture modes for BOR specimen and ROR specimen are shown in Figure 11 (a) and (b) respectively. Multiple radial cracks appear in the fractured BOR specimen and the fracture origin is right at the center of the plate beneath the loading indenter. For ROR loading condition, cross cracks formed in the inner ring area. The stress distribution outside of the inner ring is mainly circular stress perpendicular to the radius direction. Radial cracks are driven in this region, similar to BOR fracture pattern. For numerical models, the failure mechanism can be reproduced for both specimens. However, the cracks density of BOR specimen is much lower than real observations. The numerical prediction for ROR test is more realistic and both the inner crossed cracks and outer radial cracks can be clearly seen.
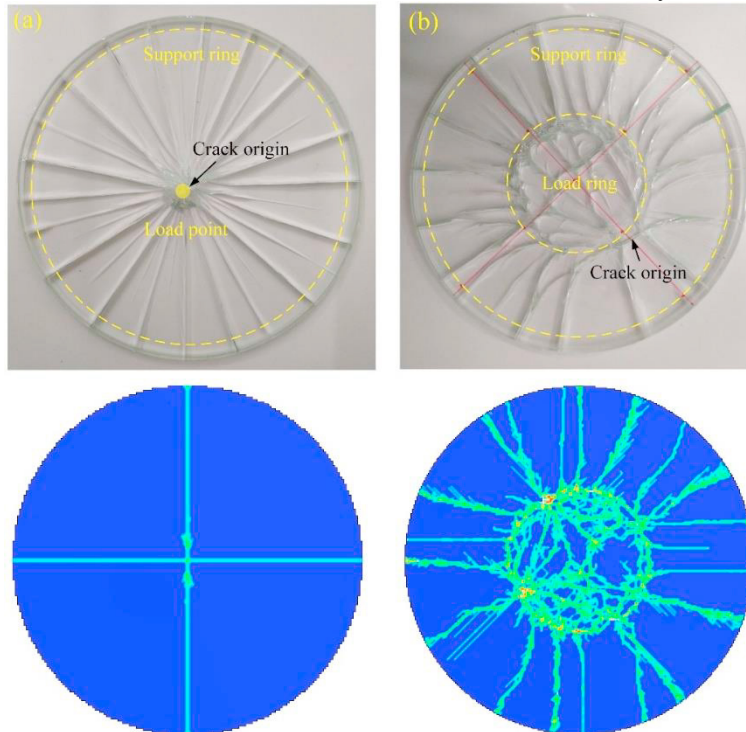

Fig. 11. Fracture modes for (a) BOR and (b) ROR specimens from tests and numerical simulations

5. Conclusions

In this study, the smeared fixed crack finite element method was utilized to represent the discontinuous macrocrack brittle behavior of aluminosilicate glass. This numerical method was carefully assessed and the numerical parameters were calibrated, including the effect of integration points, mesh size and loading speed on the numerical results. The capability of this model was evaluated by comparing the results of the numerical simulations with the corresponding BOR and ROR experimental results. During the loading process, a uniform principal strain and principal stress field were formed below the loading ring in ROR tests, while a gradient distribution was built for BOR loading condition. Finally, both the deformation field, principal strain distribution and fracture morphologies of the plate specimens could be replicated via the proposed numerical method.

Acknowledgements

References

de With, G., Wagemans, H.H.M., 1989. Ball-on-ring test revisited. J. Am. Ceram. Soc. 72, 1538–1541.

Deland, D., Zhang, Z., Kirane, K., 2020. Biaxial flexural failure of woven composite plates investigated by the ring on ring bending test. Thin-Walled Struct. 148, 106585.

Hillerborg, A., Modéer, M., Petersson, P.E., 1976. Analysis of crack formation and crack growth in concrete by means of fracture mechanics and finite elements. Cem. Concr. Res. Pergamon. https://doi.org/10.1016/0008-8846(76)90007-7

Ma, D., Esmaeili, A., Manes, A., Sbarufatti, C., Jiménez-Suárez, A., Giglio, M., Hamouda, A.M., 2020. Numerical study of static and dynamic fracture behaviours of neat epoxy resin. Mech. Mater. 140, 103214.

Mardalizad, A., Saksala, T., Manes, A., Giglio, M., 2020. Numerical modeling of the tool-rock penetration process using FEM coupled with SPH technique. J. Pet. Sci. Eng. 189, 107008.

Pelfrene, J., Van Dam, S., Sevenois, R., Gilabert, F., Van Paepegem, W., 2016. Fracture simulation of structural glass by element deletion in explicit FEM, in: Challenging Glass Conference Proceedings. pp. 439–454.

Quinn, G.D., 2016. Fractography of ceramics and glasses. National Institute of Standards and Technology Washington, DC.

Scazzosi, R., Giglio, M., Manes, A., 2020. FE coupled to SPH numerical model for the simulation of high-velocity impact on ceramic based ballistic shields. Ceram. Int.

Standard, A., 2005. Standard test method for monotonic equibiaxial flexural strength of advanced ceramics at ambient temperature. Stand. ASTM C1499-04, West Conshohocken.

Vocialta, M., Corrado, M., Molinari, J.F., 2018. Numerical analysis of fragmentation in tempered glass with parallel dynamic insertion of cohesive elements. Eng. Fract. Mech. 188, 448–469. https://doi.org/10.1016/j.engfracmech.2017.09.015

Wang, X.F., Yang, Z.J., Yates, J.R., Jivkov, A.P., Zhang, C., 2015. Monte Carlo simulations of mesoscale fracture modelling of concrete with random aggregates and pores. Constr. Build. Mater. 75, 35–45.

Wang, Z., Fu, J., Manes, A., 2021a. Discrete fracture and size effect of aluminosilicate glass under flexural loading: Monte Carlo simulations and experimental validation. Theor. Appl. Fract. Mech. 111, 102864.

Wang, Z., Ma, D., Suo, T., Li, Y., Manes, A., 2021b. Investigation into different numerical methods in predicting the response of aluminosilicate glass under quasi-static and impact loading conditions. Int. J. Mech. Sci. 196. https://doi.org/10.1016/j.ijmecsci.2021.106286

Wang, Z., Ren, T., Suo, T., Manes, A., 2021c. Quasi-static and low-velocity impact biaxial flexural fracture of aluminosilicate glass — An experimental and numerical study. Thin-Walled Struct. 165, 107939. https://doi.org/10.1016/j.tws.2021.107939

Wereszczak, A.A., Ferber, M.K., Musselwhite, W., 2014. Method for identifying and mapping flaw size distributions on glass surfaces for predicting mechanical response. Int. J. Appl. Glas. Sci. 5, 16–21.

You, Z., Zhang, M., Liu, F., Ma, Y., 2021. Numerical investigation of the tensile strength of loess using discrete element method. Eng. Fract. Mech. 247, 107610. https://doi.org/10.1016/j.engfracmech.2021.107610